POLITECNICO DI TORINO

Collegio di Ingegneria Chimica e dei Materiali

Master of Science Course
in Materials Engineering for Industry 4.0

Master of Science Thesis

Evaluation of Wear Mechanisms in Glass-Composite Prosthodontic Prostheses



Tutors

Prof. Gianfranco Genta
Dott. Giacomo Maculotti
Dott. Edoardo Goti

Candidate

Nicola Favero

September 2026

Abstract

Fixed dental prostheses are subject to multiple failure mechanisms, among which occlusal wear stands out as a particularly insidious long-term threat, since it can initiate cracks that progressively reduce the fracture resistance of the restoration. Glass-ceramic composites, owing to their favorable strength-to-weight ratio, aesthetic translucency, and chemical stability, represent an increasingly attractive alternative to conventional metal and ceramic prosthetic materials, motivating a deeper understanding of their tribological performance. This thesis presents a characterization of wear mechanisms in two glass-composite materials, G1 and G3, tested via pin-on-sample tribometry under a constant load at different sliding distances. Both removed and displaced material volumes were determined through confocal microscopy by subtracting pre- and post-tribological test surface topographies, allowing for an accurate isolation of the wear track and a clear distinction between material worn away from the surface and material merely plastically deformed during sliding. The results reveal a clear transition in wear behavior, marking the boundary between an initial running-in regime, characterized by high and material-dependent wear rates due to the removal of native surface asperities, and a subsequent stable regime in which wear rates decrease markedly for both materials. Statistical analysis confirmed that sliding distance and material significantly influence wear volume, with no significant interaction effect, while the coefficient of friction remained stable and statistically equivalent between the materials across the entire test. Overall, material G3 exhibited superior wear resistance compared to G1, particularly in the initial running-in phase, while showing comparable frictional behavior. These findings suggest that the most critical window for material selection lies within the initial service life of the restoration, when high localized stresses and surface conditioning effects act as primary drivers for early defect generation, whereas long-term wear performance appears to be governed by mechanisms common to both compounds.

Contents

1 Introduction 5
- 1.1 Causes of Dental Prosthesis Failure . . . 6
- 1.2 Wear in dental prostheses - occlusal wear . . . 6
- 1.3 Estimation of the Annual Sliding Distance from In-Vivo Kinematics . . . 7
- 1.4 Wear Mechanisms in Ceramic Dental Materials . . . 7
  - 1.4.1 Adhesive Wear . . . 8
  - 1.4.2 Tribo-oxidative Wear . . . 8
  - 1.4.3 Abrasive Wear . . . 9
  - 1.4.4 Wear by Contact Fatigue . . . 9
  - 1.4.5 Relevance to the Oral Environment . . . 9
- 1.5 Influence of Surface Topography on Wear Mechanisms . . . 10
- 1.6 State of the art . . . 11
- 1.7 Aim of the Thesis . . . 12

2 Materials and Methods 13
- 2.1 Materials . . . 13
- 2.2 Tribological Test Setup and Procedure . . . 14
- 2.3 Surface Topography Measurement . . . 16
- 2.4 Selection of Sliding Distances . . . 16
- 2.5 Surface Roughness of the Samples . . . 17
- 2.6 Experimental Setup . . . 17
- 2.7 Wear Volume Characterisation . . . 19

3 Results and Discussions 21
- 3.1 Wear Volume Evolution and Uncertainty Analysis . . . 21
- 3.2 Linear Regression . . . 25
  - 3.2.1 Verification of Function Continuity at 25 m . . . 25
- 3.3 Statistical Analysis of Wear Rates: Two-Sample t-tests . . . 26
- 3.4 Friction Coefficient and Uncertainty Analysis . . . 28
- 3.5 Statistical Analysis of Friction: Two-Way ANOVA . . . 31

4 Conclusion 33

Bibliography 35

A Experimental Wear Data Tables 37
- A.1 Sample Series G1 . . . 37
- A.2 Sample Series G3 . . . 39

B Experimental Friction Data Tables 41
B.1 Sample Series G1 41
B.2 Sample Series G3 42

C Experimental Roughness Data Tables 43

D Test Setup Procedure 45

Chapter 1

Introduction

Fixed dental prostheses represent a cornerstone of modern dental restoration and are defined as restorations that permanently replace one or more missing teeth by anchoring to adjacent natural teeth or to implants. However, when prostheses or restorations fail, the consequences can be severe, ranging from secondary caries and pulpitis to nerve damage, excessive wear of the antagonist dentition, surface degradation, aesthetic failure and, ultimately, fracture or structural failure [1]. Among the problems described above, occlusal wear deserves particular attention, as it consists of the progressive loss of material from the occlusal surfaces of the teeth, generated by the continuous friction and mechanical loads that develop during normal oral functions. This constant rubbing leads to the formation of so-called wear facets, i.e. small flat and polished areas where the enamel, or the prosthesis coating, is worn away. The appearance of these facets in a mild form is a physiological and entirely natural occurrence, related to normal mastication, and is found in both natural teeth and prosthetic restorations. However, the picture changes drastically in the presence of pathological wear, caused predominantly by bruxism (involuntary and audible grinding of the teeth) and clenching (the static, prolonged and forceful contraction of the masticatory muscles without tooth sliding). These conditions, often triggered by factors related to stress, anxiety or malocclusion, subject the materials to extreme mechanical stresses. Over time, these parafunctions can lead to functional impairment, severe sensitivity and the onset of infections, particularly once the surface layer is completely removed and the underlying dentin remains exposed [2].
Nonetheless, during normal oral function, these materials are continuously subjected to sliding contact, friction and wear against antagonist teeth and restorations, making an in-depth tribological characterization essential. To this end, a systematic approach was adopted in this study to quantify wear volume with high precision. [3] [4] Consequently, it is essential to carefully evaluate wear rates, which are governed by a complex interaction between the material's microstructure, bite force [5], and various other tribological and clinical factors [6]. Materials with a ceramic component, widely used in fixed prostheses for their excellent aesthetic and mechanical properties, present a specific challenge in this regard. On one hand, their relatively high hardness can, in extreme cases, accelerate wear of the natural antagonist dentition. On the other hand, their intrinsic brittleness means that wear facets can act as initiation sites for crack propagation, ultimately compromising the structural integrity of the restoration. Understanding how wear damage evolves at the microstructural level is therefore crucial for the optimization of dental materials for prosthetic applications [3]. Within this framework, the present study focuses on glass-ceramic composite materials, which have gained increasing relevance in restorative dentistry thanks to their unique combination of high strength-to-weight ratio, aesthetic translucency and chemical stability. These properties make them a valid alternative to

traditional metal or monolithic ceramic solutions; furthermore, their ability to faithfully mimic the natural appearance of teeth considerably improves patient acceptance and satisfaction.



Figure 1.1. Illustration of a fixed dental prosthesis used to restore missing teeth by anchoring to the adjacent prepared natural teeth.

1.1 Causes of Dental Prosthesis Failure

Among the factors that compromise the long-term success of fixed dental prostheses, mechanical, biological, and aesthetic complications are consistently identified in the literature as the most clinically significant categories of failure. Mechanical complications constitute the leading cause of prosthetic failure, accounting for 40% of failures in fixed dental prostheses (FDPs). These include debonding and loss of retention, and are strongly influenced by predisposing factors such as parafunctional habits (bruxism and clenching), occlusal prematurity, and inadequate tooth preparation [1]. Biological complications represent the second most significant cause of failure, accounting for approximately 20% of failures in both FDPs and single crowns, and affect the dental and periodontal tissues supporting the prosthesis. Biological complications include secondary caries, coronal or radicular fracture of the abutment tooth, endodontic (root canal) failure, periapical lesions, and periodontal complications [1]. Among these three categories, aesthetic failures are the least frequent, accounting for approximately 11% of failures in FDPs, and were most strongly associated with restorations in service for less than 6 months [1]. They include colour mismatch with adjacent natural teeth, overcontouring, metal exposure in (Porcelain-Fused-to-Metal) restorations, and porcelain chipping that simultaneously compromises both appearance and function [1].

1.2 Wear in dental prostheses - occlusal wear

Among the failure mechanisms outlined above, occlusal wear deserves particular attention, as it represents a mechanical form of wear that is often insidious and underestimated as a long-term cause of prosthetic failure. Occlusal wear refers to the progressive loss of dental substance resulting from the direct frictional contact between opposing teeth during function. As reported by Borrero-Lopez et al., occlusal wear can become life-limiting not merely through progressive

material loss, but because wear facets act as crack initiation sites that propagate into the underlying structure, progressively reducing the residual fracture resistance of the prosthesis [3]. Furthermore, hard ceramic materials such as zirconia have been shown to accelerate wear of the opposing natural dentition, raising additional long-term clinical concerns [3]. It is therefore on this specific failure mechanism — occlusal wear — that the present work focuses, aiming to characterise its progression and assess its impact on the mechanical integrity of ceramic-based dental restorations.

1.3 Estimation of the Annual Sliding Distance from In-Vivo Kinematics

In order to correctly reproduce the frictional sliding motion between opposing teeth during mastication in a laboratory setting, it was necessary to determine the physiological extent of tooth sliding from the existing literature. To ensure that the testing parameters chosen for this study accurately reflect the in-vivo environment, they were derived directly from the known kinematics of the human masticatory system, as outlined below.

Regarding the sliding distance per mastication cycle, independent clinical and tribological studies indicate a consensus range of 0.9 mm to 1.5 mm. Specifically, gnathographic measurements by Rilo et al. revealed a mean contact glide of 1.38 mm to 1.46 mm during the closing masticatory stroke, with no statistically significant difference across different food textures (e.g., chewing gum, soft bread, and peanuts) [7]. This aligns with the widely accepted central tendency of 0.9 to 1.2 mm reported in comprehensive reviews by Branco et al. and Lewis and Dwyer-Joyce [8].

Concurrently, the average number of tooth-to-tooth occlusal contacts is widely established in wear lifetime prediction models at a nominal baseline of approximately 1×10^6 cycles per year [2]. This standard order of magnitude is corroborated by time-based estimations: considering that each sliding contact lasts approximately 0.25 to 0.33 seconds, a daily functional loading of 15 min –30 min translates to roughly 1.1 to 2.2 million annual cycles [9]. While this cycle count is subject to further increase due to variability factors such as diet, prosthodontic status, and parafunctional habits like bruxism [9], the conservative baseline of 1×10^6 cycles is typically adopted for standardized wear calculations.

By combining these physiological metrics (the conservative 1×10^6 cycles per year and the 1.0–1.5 mm of sliding per cycle), the estimated annual cumulative net sliding distance between opposing teeth amounts to 1,000 m to 1,500 m.

1.4 Wear Mechanisms in Ceramic Dental Materials

Wear is defined as the progressive damage of a surface in intimate contact with another, resulting in the formation of fragments that leave the tribological system. Wear may cause direct functional failure, reduce dimensional tolerances and surface quality, or induce surface damage that acts as a precursor to subsequent structural failure of the component. The nature of the relative motion between two bodies in contact determines which wear process is dominant: sliding, rolling, rolling-sliding, fretting, abrasion, and erosion are among the most common configurations encountered in practice.

Despite this variety, the investigation of wear damage is simplified by the observation that

each wear process is governed by one of four fundamental mechanisms: adhesive wear, tribo-oxidative wear, abrasive wear, and wear by contact fatigue. Each of these is described below, with particular attention to their relevance in brittle materials such as ceramics.

1.4.1 Adhesive Wear

Adhesive wear occurs when adhesion forces between contacting asperities play a predominant role in the detachment of wear fragments. In brittle materials such as ceramics, which are characterized by low fracture toughness K_{IC}, a specific mechanism applies: the adhesive interaction at asperities induces a surface tensile stress during sliding, which can propagate pre-existing micro-cracks and generate wear fragments through brittle fracture rather than plastic deformation. For a contact between a sphere and a plane, setting $\nu = 0.25$ (typical for ceramic materials), the maximum tensile stress at the surface is approximated as:

$$\sigma_t \approx \frac{P_{\max}}{6}(1+10\mu) \tag{1.1}$$

where $P_{\max}$ is the maximum contact pressure and μ is the friction coefficient. If a surface micro-crack of length c is present at the edge of the contact area, brittle fracture is initiated when σ_t reaches the critical value σ_F, given by fracture mechanics as:

$$\sigma_F = \frac{K_{IC}}{1.12\sqrt{\pi c}} \tag{1.2}$$

Combining Eq. 1.1 with the fracture condition $\sigma_t \geq \sigma_F$, the condition for adhesion-induced brittle wear becomes:

$$P_{\max} \geq \frac{5.36\,K_{IC}}{\sqrt{\pi c}(1+10\mu)} \tag{1.3}$$

The crack length c is closely related to the grain size of the microstructure, since defects such as pores are mainly located at grain boundaries. As a practical example, setting $c = 10\,\mu$m, $K_{IC} = 2\,\text{MPa}\,\text{m}^{1/2}$ and $\mu = 0.4$, wear onset occurs at $P_{\max} \approx 380\,$MPa. When the applied pressure exceeds the threshold defined by Eq. 1.3, massive fragmentation occurs, producing blocky or plate-like debris on the scale of the grain size, with correspondingly high wear rates and friction coefficients. Below this threshold, fragmentation is confined to asperity tips and the wear mechanism typically transitions to a milder abrasive regime, resulting in significantly lower wear rates. [10]

1.4.2 Tribo-oxidative Wear

Tribo-oxidative wear arises from the interaction of contacting surfaces with an oxygen-containing environment. It results from the combined action of oxidative chemical reactions and mechanical stresses at the asperities. In many metallic systems, this mechanism leads to the formation of a surface oxide layer that limits direct metal-to-metal contact and acts as a solid lubricant, thereby reducing both friction and wear. Unlike metals, which readily react with environmental oxygen under the mechanical stresses of sliding, ceramic dental materials are inherently composed of stable oxides (such as the silica and lithia networks characterizing the glasses studied here). Consequently, direct tribo-oxidative reactions play a negligible role in their overall wear behavior. [10]

1.4.3 Abrasive Wear

Abrasive wear occurs when a hard particle or surface protuberance penetrates and grooves a softer counterface. Two configurations are distinguished:

- **Two-body abrasion**: hard particles are embedded in one of the contacting surfaces and act directly on the opposing material, producing grooves through plastic deformation or brittle fracture.
- **Three-body abrasion**: loose particles trapped between the two surfaces are free to rotate, resulting in a less severe but still significant material removal.

In brittle materials, abrasive interactions produce wear fragments, and damage is described through the *Lawn–Swain mechanism*: hard angular particles indent the surface, generating lateral cracks that propagate almost parallel to the surface and eventually cause spallation of material. For this to occur, the hardness of the abrasive particles must be at least 20–30% greater than that of the abraded surface. Various models have been proposed to quantify the abrasive wear rate of brittle materials. The *Evans–Marshall model*, based on the Lawn–Swain mechanism, expresses the volumetric wear rate W as:

$$W \propto \frac{P^{9/8}}{H^{1/8} K_{\mathrm{IC}}^{1/2}} \tag{1.4}$$

where P is the applied normal load, H is the material hardness, and K_{IC} is the fracture toughness. This relationship highlights that materials with low fracture toughness K_{IC} are particularly vulnerable to abrasive wear. Furthermore, microstructural features play a critical role: weak grain boundaries can anticipate brittle fracture through grain ejection, at stress levels below those predicted by continuum models. [10]

1.4.4 Wear by Contact Fatigue

Unlike adhesive or abrasive wear, which involve continuous and progressive material removal from the onset of sliding, wear by contact fatigue is fundamentally a threshold phenomenon driven by cyclic loading. Under repeated mechanical stress, damage accumulates progressively over time until a critical limit is reached, corresponding to the fatigue life of the loaded region. In hard and brittle materials like ceramics, where macroscopic plastic deformation is practically absent, this process is characterized by subsurface crack nucleation and propagation rather than plastic flow. Eventually, these subsurface cracks coalesce, leading to the sudden detachment of wear fragments in the form of localized spalling or pitting. This intermittent release of material clearly distinguishes the contact fatigue mechanism from the continuous grooving or shearing typical of other wear modes. The severity of this mechanism is governed by numerous factors, including the amplitude of cyclic contact stresses, the lubrication regime, material fracture toughness, microstructural cleanliness, and residual stresses. [10]

1.4.5 Relevance to the Oral Environment

Among the mechanisms described above, tribo-oxidative effects and contact fatigue are of particular relevance to the oral environment. The presence of saliva and moisture introduces chemical interactions that, even in the absence of direct oxidation, can influence the surface degradation of ceramic restorations: water molecules adsorb at crack tips and promote stress corrosion.

This effectively reduces the critical stress intensity factor (K_{IC})—the intrinsic threshold defining the material's resistance to crack propagation—and accelerates subcritical crack growth [10]. This effect compounds with the repetitive nature of masticatory loading, which typically involves several hundred thousand contact cycles per year. Cyclic Hertzian contact stresses, combined with moisture-driven stress corrosion at crack tips, can progressively degrade ceramic restorations even at stress levels well below the static fracture threshold (σ_F), which represents the critical load required to cause sudden, catastrophic failure in a single event. The clinical manifestation of this combined process is the detachment of surface fragments, observed as chipping or delamination of the prosthetic restoration [10].

1.5 Influence of Surface Topography on Wear Mechanisms

To fully understand the evolution of tribological phenomena and accurately quantify the damage, it is fundamental to establish that the initial topography of the sample cannot be considered negligible. The real surface is never perfectly smooth, but is rather the result of the superposition of geometric irregularities at different spatial scales [11]. Specifically, surface topography is characterized of four main components: form, waviness, roughness, and microroughness [11].

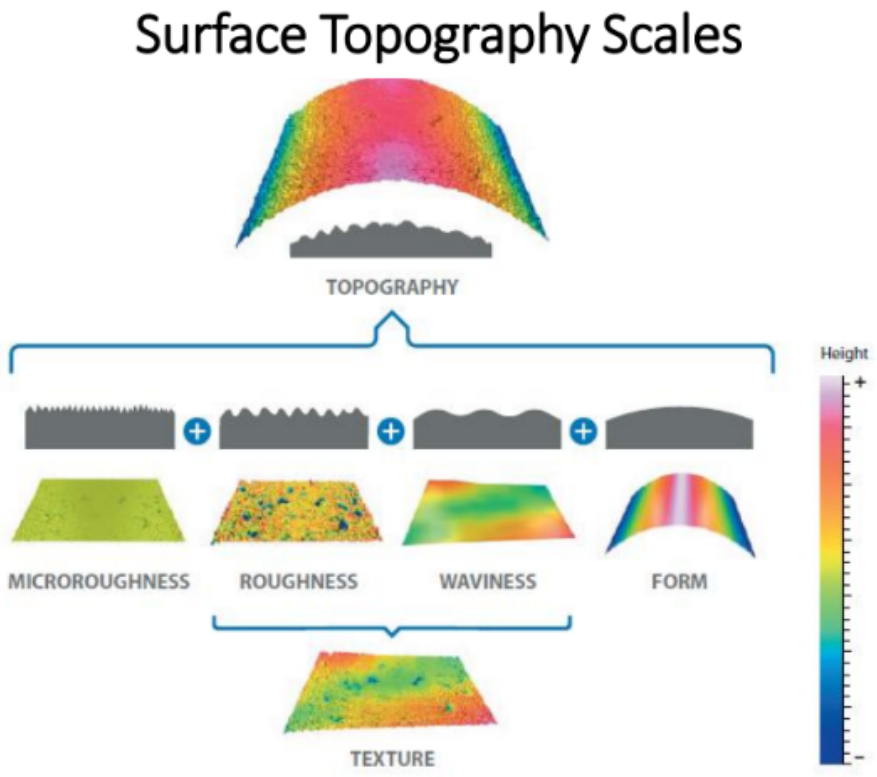


Figure 1.2. Representation of the four main components of surface topography: form, waviness, roughness, and microroughness.

Form represents the lowest spatial frequency component, defined by macroscopic deviations from the ideal geometry caused by machine tool errors or, as in the case of dental prostheses, by the intrinsic anatomical design of the component. Waviness is a medium spatial frequency deviation superimposed on the form, usually induced by transient cyclic factors during the manufacturing process, such as machine-tool vibrations. Roughness constitutes the high

spatial frequency component, directly determined by the cutting tool action or the surface finishing process. Finally, microroughness represents the irregularities at the shortest scale, strictly related to the intimate microstructure of the material. The coexistence of these geometric characteristics introduces considerable complexity in the quantitative evaluation of wear. From the perspective of contact mechanics, when two surfaces slide against each other, the real contact does not occur over the entire nominal area, but is exclusively concentrated at the summits of the geometric asperities (the peaks of the profile). Consequently, the local contact pressures at the interface reach extremely high values, generating severe stress states on the peaks. This phenomenon governs the so-called *running-in* phase, during which the most pronounced asperities undergo rapid plastic deformation, are removed by shearing (abrasive wear), or undergo brittle micro-cracking, a mechanism particularly relevant in ceramic materials characterized by low fracture toughness. In light of these considerations, profilometric analysis is an essential and indispensable tool for the correct characterization of component wear. This approach is even more critical in the field of fixed dental prostheses, where the functional surface is not flat but presents a complex and well-defined anatomical macro-form. Without an adequate signal filtering strategy to separate the macroscopic form and the initial roughness from the actual tribological damage, it would be impossible to reliably isolate and quantify the true volume of removed material during the service of the prosthesis.

1.6 State of the art

Current research on dental tribology studies friction, wear, and lubrication in the contacts between natural teeth, restorations, and opposing teeth, with the aim of understanding how materials wear and how to design more durable restorations. [12] [13] The most cited works define the field as a cross between oral biology, dental materials, and wear and fracture simulation of brittle solids. What emerges is that wear varies greatly from patient to patient, depending on the diet, the lifestyle and the oral care. In many cases, wear does not immediately compromise the teeth function, but becomes primarily an aesthetic issue or a progressive loss of occlusal height; in severe cases, however, it can contribute to sensitivity, loss of function, and fractures. [13] [3] In terms of materials, ceramics are a central focus of the literature because they are widely used in prosthetics and crowns. Their tribological behavior depends on microstructure, toughness, and surface finish. The most stable consensus is that ceramics tend to have low material wear but can increase wear on the opposing tooth, especially enamel. Among ceramics, zirconia is often described as very wear-friendly toward the opposing tooth, and a polished surface tends to yield better results than a glazed surface. [3] [8] [14] In the experimental work on ceramic materials, zirconia exhibits the lowest wear rates, while lithium disilicate is among the most vulnerable; furthermore, the microstructure controls the detachment and microfracture mechanisms. Resin composites tend to exhibit greater long-term wear than ceramics, and their behavior depends largely on the cohesion of the organic matrix, the nature of the fillers, and their detachment or protrusion on the surface. The literature emphasizes that exposed or detached filler particles become a significant cause of abrasion of the opposing enamel. Metallic restorations tend to wear the opposing tooth less than other classes of materials because they have low relative hardness and high ductility, with a prevalence of plastic deformation and adhesive wear. [8]. Given that lithium-disilicate-based materials are consistently reported as more prone to wear than zirconia, and that microstructure is recognized as the governing factor in their detachment and microfracture behaviour, characterising how compositional variations within this same glass-ceramic system affect wear resistance becomes particularly relevant. Another important area of concern is that of natural enamel wear. The key issue here is not only the loss of material,

but also the fact that wear can increase susceptibility to fracture by introducing surface defects and lowering the critical loads for crack propagation. [3] [9] The literature strongly emphasizes that laboratory tests must mimic occlusal contact, but no setup perfectly reproduces the real mouth. This is why various wear simulators have been developed, including pin-on-disk configurations, chewing simulators, and ball-on-3-specimens. The latter is widely used because it produces almost circular wear scars reminiscent of clinical veneers and allows for a relatively simple estimate of the stable wear rate. This is one of the reasons why the dental literature does not treat wear as simple "consumption," but as a process coupled with fatigue, microcracking, and brittle fracture. [3] [13] The experimental literature on dental wear is characterized by a significant lack of standardization: numerous test protocols have been proposed, but only a few have been rigorously validated, and their correlation with clinical wear behavior remains moderate at best. Several open questions continue to limit progress in the field. The first concerns precisely this absence of standardized testing procedures, which makes it difficult to compare results across studies and to draw generalizable conclusions. The second is the need for long-term clinical data: much of the available evidence is derived from in vitro experiments, and its translation to clinical practice is not always straightforward, as laboratory conditions inevitably simplify the complexity of the oral environment. The third, and perhaps most fundamental, open question concerns the relative contribution of the many variables that govern wear behavior. Parameters such as microstructure, surface finish, applied load, motion kinematics, saliva composition, and antagonist material all interact simultaneously, making it difficult to isolate the effect of any single factor. This complexity is further compounded by the high variability between patients in terms of bite force, occlusal habits, salivary flow, and bruxism severity. As a result, it remains unclear whether the longevity of a prosthesis is primarily determined by a specific mechanical property of the material, or whether it is the combined effect of all these variables that governs the transition from mild surface wear to more severe damage modes such as chipping, microcracking, and bulk fracture.

1.7 Aim of the Thesis

The primary aim of this thesis is to comprehensively characterize the wear behavior and tribological lifespan of two glass-ceramic composite materials (G1 and G3) belonging to the Li_2O–SiO_2 system. Since occlusal wear represents a critical factor determining the long-term clinical viability of dental restorations, understanding the deterioration mechanisms of these composites is essential to validate their medical application for permanent tooth replacement. Specifically, this study seeks to quantitatively evaluate the progression of wear volume under simulated masticatory loading across varying sliding distances, using an artificial saliva solution to replicate the oral environment. By employing advanced 3D confocal microscopy and a pin-on-sample tribometer to map the resulting wear tracks, the research aims to accurately isolate the true volume of removed material. This volumetric data is then utilized to compute the specific Archard wear rates, providing a standardized metric for a precise analysis of the transition between the severe initial *running-in* phase and the stabilized *stable* wear regime. Furthermore, the study investigates the correlation between native surface topography, dynamic friction coefficients, and overall wear rates. Ultimately, the goal is to determine whether these innovative glass-ceramic composites possess sufficient tribological durability and mechanical reliability to act as safe, effective, and long-lasting clinical alternatives to traditional prosthetic materials.

Chapter 2

Materials and Methods

The wear behaviour of a material under sliding contact is governed by a combination of factors, among which the intrinsic nature of the material, the surface roughness of the contacting bodies, and the specific experimental conditions under which the test is conducted (e.g., applied load, sliding distance, and environment). Before presenting the tribological results of this study, it is therefore necessary to characterise the materials under investigation and their native surface finish, as these factors provide the mechanical and microstructural basis for interpreting the wear response observed in the following chapters.

2.1 Materials

The two glass-ceramic composites investigated in this study, G1 and G3, belong to the Li_2O–SiO_2 system, one of the most extensively studied glass-ceramic (GC) families for dental applications owing to its exceptionally favourable combination of physical, chemical, mechanical, and optical properties, with modifying oxides (Al_2O_3 and K_2O) added to tailor structure and properties [15]. The detailed molar compositions of the experimental glasses are summarized in Table 2.1.

Table 2.1. Detailed molar compositions (mol.%) and SiO_2/Li_2O molar ratios of the experimental glass-ceramic composites G1 and G3.

Material	**SiO_2 [mol.%]**	**Li_2O [mol.%]**	**K_2O [mol.%]**	**Al_2O_3 [mol.%]**	**SiO_2/Li_2O ratio**
G1	74.30	15.23	5.24	5.24	4.88
G3	71.78	22.96	2.63	2.63	3.13

The starting glasses are considerably richer in silica than the stoichiometric lithium disilicate composition ($Li_2Si_2O_5$, LS2, SiO_2/Li_2O molar ratio of 2:1), with G1 and G3 exhibiting SiO_2/Li_2O molar ratios of 4.88 and 3.13, respectively [15]. Despite this silica-rich starting composition, lithium disilicate remains the targeted final crystalline phase, valued for the mechanical and optical properties it confers to dental restorations. During devitrification, lithium metasilicate (Li_2SiO_3, LS) frequently precipitates first as an intermediate or secondary phase, particularly in more heavily modified compositions such as G1, before reacting with the surrounding silica-rich glassy matrix to transform into the final lithium disilicate phase [15]. From a structural standpoint, Li_2O–SiO_2 glasses containing less than 30 mol.% Li_2O tend to exhibit opalescence or opacity upon cooling, due to phase separation resulting in the segregation of

Li-rich droplet zones within a SiO_2-rich glass matrix. At a stoichiometric composition of 33.3 mol.% Li_2O (SiO_2/Li_2O ratio of 2:1), the droplet and surrounding phases reach identical composition, yielding the most structurally homogeneous lithium disilicate (LS2) glass. In practice, however, the addition of secondary oxides to improve chemical durability and mechanical performance has led to the widespread use of non-stoichiometric LS2 compositions. Notably, the first GC based on the Fotoform® material was developed by Stookey using a photosensitive glass with a SiO_2/Li_2O molar ratio of 3.8:1.0, marking a foundational milestone in the field. [16]

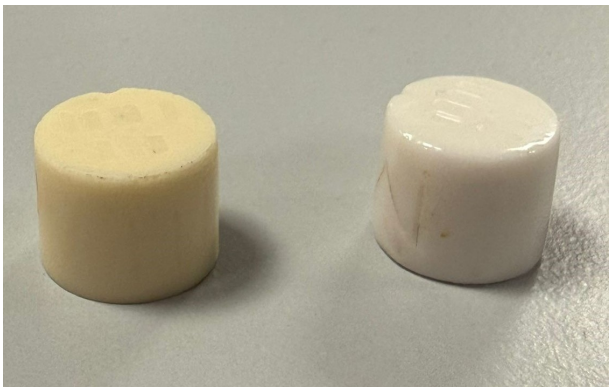


Figure 2.1. Glass-ceramic composite specimens (Li_2O–SiO_2 system). On the left, the material G3 with a matte finish ; on the right, the material G1 with a glossier finish.

2.2 Tribological Test Setup and Procedure

The tribological characterization was performed using a state-of-the-art Anton Paar TRB tribometer.

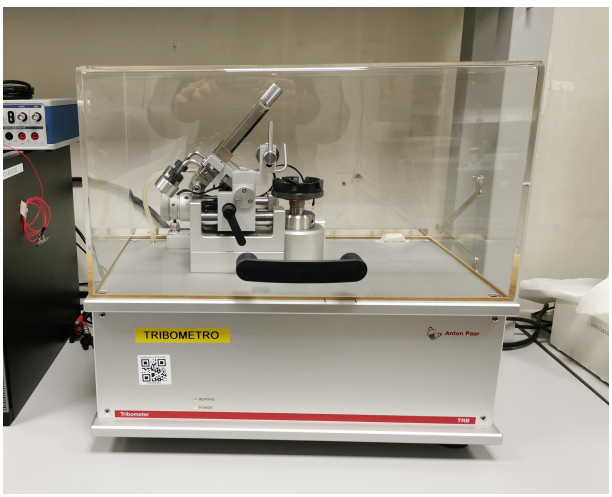


Figure 2.2. Overall view of the Anton Paar TRB tribometer utilized for the tribological characterization of the glass-ceramic composites.

In addition to recording the applied normal and tangential forces, the tribometer continuously acquired the coefficient of friction throughout each test, allowing its evolution to be tracked over the entire sliding distance and correlated with the corresponding wear behaviour. For the

purpose of this study, pin-on-sample tests were carried out in a linear sliding motion against a flat ceramic pin. The tribometer was set to reproduce a linear reciprocating stroke of 1.5 mm per cycle, corresponding to the upper bound of the physiological sliding distance range identified from the literature (see Section 1.3), so as to generate a wear track representative of the sliding contact occurring between opposing teeth during mastication. A constant normal load of 10 N was applied. This value was selected as the maximum feasible load for the setup, since higher loads would generate excessive tangential forces, ultimately leading to the fracture of the ceramic pin.

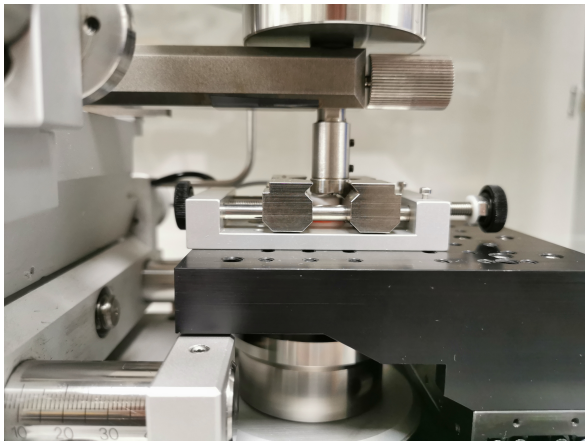


Figure 2.3. Anton Paar TRB tribometer setup utilized for the pin-on-sample wear tests.

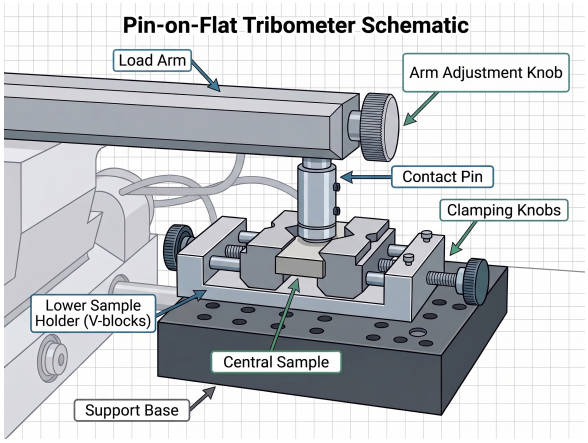


Figure 2.4. Schematic representation detailing the loading arm, contact pin, and clamping mechanism.

2.3 Surface Topography Measurement

Topographical characterization was carried out with a confocal microscopy (CSI) Sensofar S Neox with a Nikon objective (magnification 20×, numerical aperture 0.45, field of view of (1.56×1.56) mm with squared pixels of $1.56\,\mu$m side). An F-operator to perform plane correction by least-square estimation and a Gaussian L-filter with a nesting index of 0.8 mm were applied.

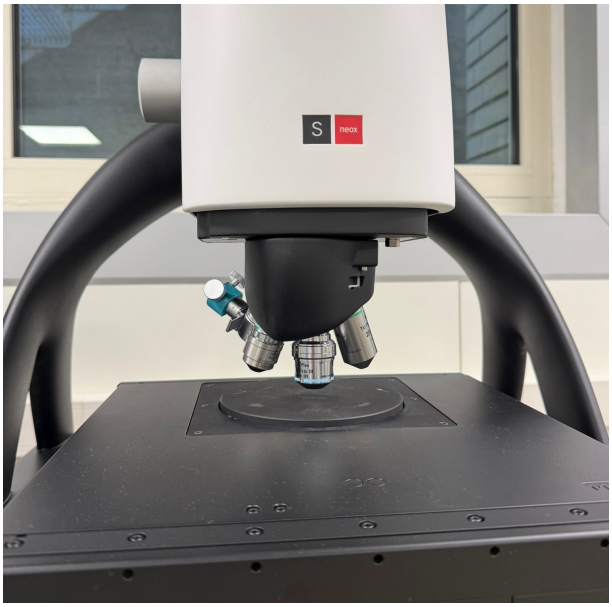


Figure 2.5. Sensofar S neox confocal microscope utilized for the 3D surface topography acquisition of the specimens before and after the tribological tests.

2.4 Selection of Sliding Distances

Building on the annual cumulative sliding distance of 1,000 m to 1,500 m estimated from the retrieved experimental and clinical literature (see Section 1.3), a set of five sliding distances (5, 15, 25, 35, and 50 m) was selected for the wear tests performed in this study, representing a practically feasible yet clinically relevant fraction of this annual range. In particular, the maximum experimental sliding distance of 50 m selected for this study corresponds roughly to the first 2 to 3 weeks of clinical service (approximately 30,000 to 50,000 masticatory cycles). This specific temporal window was deliberately chosen to strictly isolate and investigate the transient *running-in* phase. Testing the materials over an extended distance (e.g., in the kilometer range) would completely obliterate the native surface asperities, burying the initial transient wear rates under a massive volume of stable data. By limiting the test to 50 m, it was possible to precisely capture the critical period responsible for surface conditioning and initial defect generation, before the tribological system inevitably transitions into a long-term stable wear regime.

2.5 Surface Roughness of the Samples

As part of the preliminary characterization of the sample batches, statistical analysis of the native surface roughness parameters (S_a, the arithmetical mean height, and S_q, the root mean square height, the latter being more sensitive to pronounced peaks and valleys due to the squaring of the surface deviations) revealed a marked topographical difference between the two tested composites, with material G1 exhibiting a significantly smoother and more homogeneous native surface compared to G3. The complete dataset of the experimental roughness measurements is reported in Appendix C (Table C.1). Specifically, G1 features a median roughness (S_a) nearly an order of magnitude lower than G3 (0.089 μm versus 0.629 μm), accompanied by a markedly narrower data dispersion, indicative of greater microstructural regularity. The same trend is confirmed by the S_q parameter, with median values of 0.138 μm for G1 versus 1.141 μm for G3, corroborating the consistency of the observed topographical difference across both roughness descriptors. Due to this evident heteroscedasticity between the samples (the substantially unequal variance in roughness between G1 and G3, which would violate the equal-variance assumption underlying standard parametric tests), the inferential investigation was conducted via the non-parametric Mood's median test, which compares group medians without assuming normality or equal variances between groups. The test rejected the null hypothesis of equal medians with a highly significant result ($p < 0.001$, $\chi^2 = 30.00$). This confirms that the topographical discrepancy between the two groups is a structural feature of the provided samples and not attributable to random fluctuations. Since surface roughness is itself known to influence wear behaviour, this genuine and statistically confirmed difference in native surface finish provides a solid mechanical basis for anticipating a correspondingly different wear response between the two composites, a difference that will be examined in the tribological results presented later in this work.

2.6 Experimental Setup

The overall experimental workflow for each specimen followed a sequential before-after protocol. For every specimen, the native surface topography was first acquired via confocal microscopy under the settings detailed in Section 2.3, providing a reference map of the surface prior to any tribological interaction. The specimen was then subjected to the wear test, following the tribometer configuration and step-by-step setup procedure described in Section 2.2 and Appendix D. Upon completion of the test, the surface topography of the worn area was re-acquired under the same microscopy settings, so as to ensure that any observed difference could be attributed exclusively to the sliding contact, rather than to variations in the measurement conditions. The pre- and post-test topographies were then imported into MountainsMap (surface analysis software), where they were spatially aligned to a common reference frame; this alignment step is essential, since even small lateral or angular misalignments between the two acquisitions would introduce spurious differences unrelated to the actual material removal. Once aligned, the wear track was isolated and the corresponding topographical data were exported for further processing in MATLAB, where the point-by-point subtraction between the pre- and post-test surfaces was performed to obtain the effective wear volume, as detailed in Section 2.7.

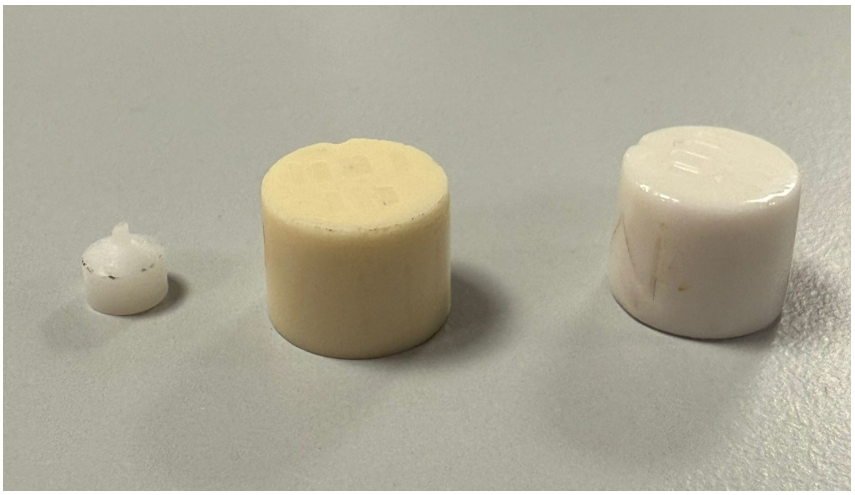


Figure 2.6. Size comparison of the physical components involved in the wear tests: the flat ceramic pin (left) and the two glass-ceramic composite specimens (center and right).

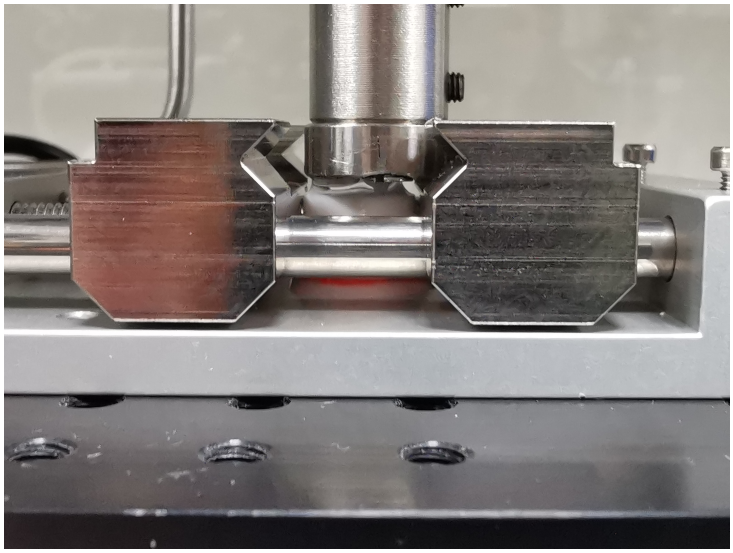


Figure 2.7. Close-up detail of the stable liquid meniscus formed by the artificial saliva solution between the ceramic pin and the specimen surface.

2.7 Wear Volume Characterisation

When evaluating the wear occurred in the samples, the initial roughness and other topographical features are not part of the tribological damage to be measured, and must therefore be removed to avoid confounding the background roughness with the actual volume of material removed. It is equally important to remove the contribution of form and noise from the post-wear topography, so as to isolate the actual wear track. There is also a methodological reason for this approach: if a partial reconstruction of the surface are used, information is lost and the wear volume may be over- or underestimated. This is because real surfaces present substantial irregularities, so it would be incorrect to assume that the surface originally present within the wear track was flat, or that it simply followed the same profile as the adjacent, unworn regions. Acquiring the full surface topography, both before and after the test, avoids this assumption and allows the pre-existing irregularities of the specimen to be properly accounted for when estimating the actual volume of material removed [17]. To operationalize this approach, as described in Section 2.6, the wear behavior is characterized by the effective wear volume (V_{eff}), obtained via a point-by-point subtraction of the pre-test topography from the post-test topography. This procedure is performed following the alignment of the two surfaces in MountainsMap and subsequent processing in MATLAB (Figure 2.8).

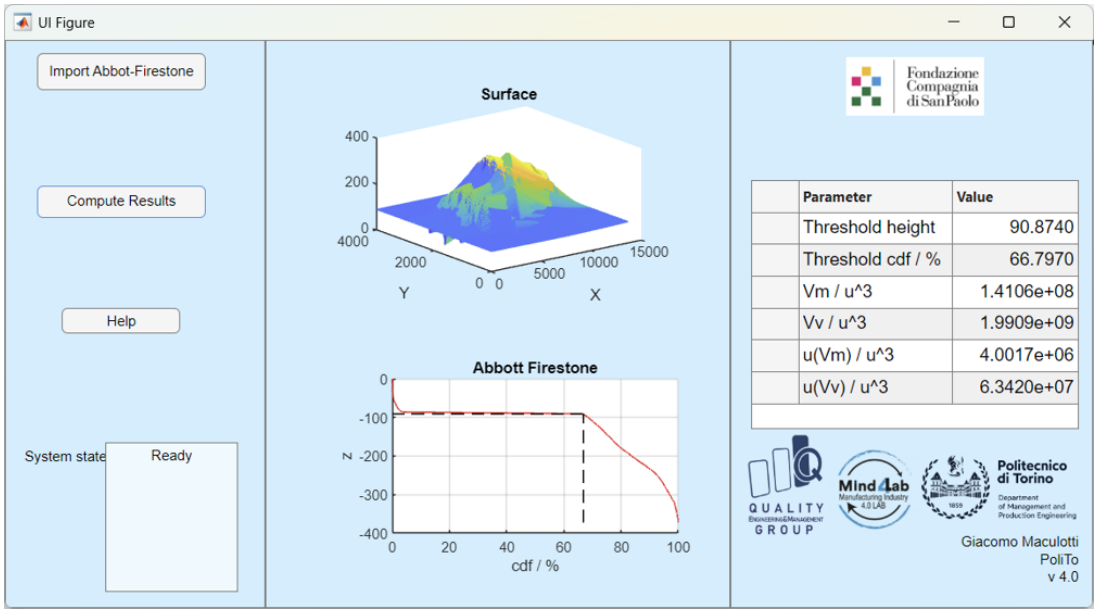


Figure 2.8. MATLAB graphical user interface employed for the processing of topographical data and the evaluation of volumetric wear parameters.

This volumetric change induced by the sliding contact does not represent a single homogeneous phenomenon, but rather comprises two physically distinct contributions. The first is the volume of material genuinely removed from the specimen (V_r), representing material permanently lost from the surface as a direct consequence of the sliding contact. The second is the volume of material that was not removed at all, but merely displaced or plastically deformed during sliding (V_p), re-emerging as pile-up ridges that protrude above the original surface level along the edges of the wear track. Since this displaced material remains attached to the specimen, failing to distinguish it from genuinely removed material would lead to a systematic underestimation of the true wear volume. The point-by-point subtraction method adopted in this study enables these two contributions to be separated and quantified independently, yielding the overall effective

damage as:

$$V_{\text{eff}} = V_r + V_p \tag{2.1}$$

The complete set of experimental data regarding the wear volumes, calculated from the pre-test and post-test surface topographies, is reported in Appendix A.
The Archard wear rates, mathematically defined as the rate of increase of the effective wear volume with respect to the sliding distance (i.e., dV_{eff}/ds), are directly estimated based on these calculated values of V_{eff}. For analytical purposes, this progression in wear volume is considered, as a first approximation, to be piecewise linear.
According to the classical Archard equation (Equation 2.2), the volume of material removed by sliding wear is proportional to the applied normal load and the sliding distance, and inversely proportional to the hardness of the softer material, via a dimensionless wear coefficient K:

$$V = K \frac{F_N s}{H} \tag{2.2}$$

where F_N is the normal load, s is the sliding distance, and H is the hardness of the material [17].

Chapter 3

Results and Discussions

3.1 Wear Volume Evolution and Uncertainty Analysis

The following tables report the wear track data extracted from the surface topography of each tested specimen, obtained by means of the point-by-point subtraction procedure described above. For each specimen, the resulting wear volume V_{eff} is reported as a function of the corresponding sliding distance, together with its associated instrumental measurement uncertainty.

Table 3.1. Experimental wear data for the G1 series specimens, including uncertainty.

MATERIAL	SPECIMEN	SLIDING DISTANCE - L [m]	WEAR VOLUME - $V_{eff,i}$ [μm^3]	u_i [μm^3]
G1	2	5	41.8614	0.0313
		15	103.8024	0.0704
		25	129.1813	0.0934
		35	162.3240	0.1026
		50	213.6451	0.1410
G1	3	5	29.5985	0.0187
		15	82.4276	0.0533
		25	137.9971	0.0853
		35	176.6622	0.0968
		50	156.7301	0.1092
G1	4	5	31.7728	0.0172
		15	86.7172	0.0528
		25	139.4206	0.0889
		35	131.0681	0.0811
		50	205.6402	0.1292

Table 3.2. Experimental wear data for the G3 series specimens, including uncertainty.

MATERIAL	SPECIMEN	SLIDING DISTANCE - L [m]	WEAR VOLUME - $V_{eff,i}$ [μm^3]	u_i [μm^3]
G3	1	5	26.1220	0.0159
		15	74.4365	0.0479
		25	119.3411	0.0753
		35	129.8414	0.0836
		50	155.4510	0.1005
G3	2	5	27.5092	0.0159
		15	52.8332	0.0324
		25	101.6076	0.0619
		35	96.7444	0.0594
		50	158.5480	0.0947
G3	3	5	20.7855	0.0106
		15	67.8223	0.0438
		25	86.0806	0.0556
		35	133.4818	0.0858
		50	175.834	0.1087

To synthesize the results obtained from the individual specimens and evaluate the statistical dispersion of the data for each specific sliding distance, the mean wear volume (m), the combined instrumental measurement uncertainty (u_{mes}), the expanded uncertainty (U), and the relative percentage uncertainty ($U_{\%}$) were calculated.
The mean wear volume m for a given test length was calculated as the arithmetic mean of the effective wear volumes measured on the three replicated samples ($V_{eff,i}$):

$$m = \frac{1}{n}\sum_{i=1}^{n} V_{eff,i} \quad [\mu\text{m}^3] \tag{3.1}$$

where $n = 3$ represents the number of specimens tested for each combination of material and distance.
To correctly propagate the instrumental error, the combined instrumental measurement uncertainty u_{mes} for the replicate group was determined as the root mean square (RMS) of the individual measurement uncertainties u_i associated with each single topographical acquisition:

$$u_{mes} = \sqrt{\frac{1}{n}\sum_{i=1}^{n} u_i^2} \quad [\mu\text{m}^3] \tag{3.2}$$

This was obtained combining metrological characteristics of the surface topography measuring instrument, calibrated as per ISO 25178-700 [4] [18].
To quantify the overall dispersion of the results, the expanded uncertainty U was evaluated by combining the sample variance (s^2) of the measured volumes with the squared instrumental measurement uncertainty (u_{mes}^2). The combined standard uncertainty was then multiplied by an expansion factor of $\frac{2}{\sqrt{3}}$:

$$U = \frac{2}{\sqrt{3}} \cdot \sqrt{s^2 + u_{mes}^2} \quad [\mu\text{m}^3] \tag{3.3}$$

where $s^2 = \frac{1}{n-1}\sum_{i=1}^{n}(V_i - m)^2$.

Finally, to facilitate the comparison of variability across the different wear phases, the relative percentage uncertainty $U_{\%}$ (dimensionless) was calculated as the ratio between the expanded uncertainty and the mean volume:

$$U_{\%} = \left(\frac{U}{m}\right) \cdot 100 \quad [\%] \tag{3.4}$$

The results of these calculations, obtained by applying the aforementioned formulas to the raw experimental data, are summarized in Table 3.3 for the G1 series and Table 3.4 for the G3 series. These tables report the computed mean wear volumes alongside their respective absolute and relative uncertainties at each evaluated sliding distance, providing a comprehensive overview of the data dispersion.

Table 3.3. Calculated values of mean wear volume and associated uncertainties for the G1 series specimens.

m [μm^3]	u_{mes} [μm^3]	U [μm^3]	$U_{\%}$ [%]
34.4109	0.0233	7.5556	21.9569
90.9824	0.0594	13.0572	14.3514
135.5330	0.0893	6.4055	4.7261
156.6848	0.0940	26.9212	17.1818
192.0051	0.1272	35.5768	18.5291

Table 3.4. Calculated values of mean wear volume and associated uncertainties for the G3 series specimens.

m [μm^3]	u_{mes} [μm^3]	U [μm^3]	$U_{\%}$ [%]
24.8056	0.0144	4.0991	16.5249
65.0307	0.0419	12.7814	19.6544
102.3431	0.0648	19.2172	18.7772
120.0225	0.0772	23.3730	19.4738
163.2777	0.1014	12.6836	7.7681

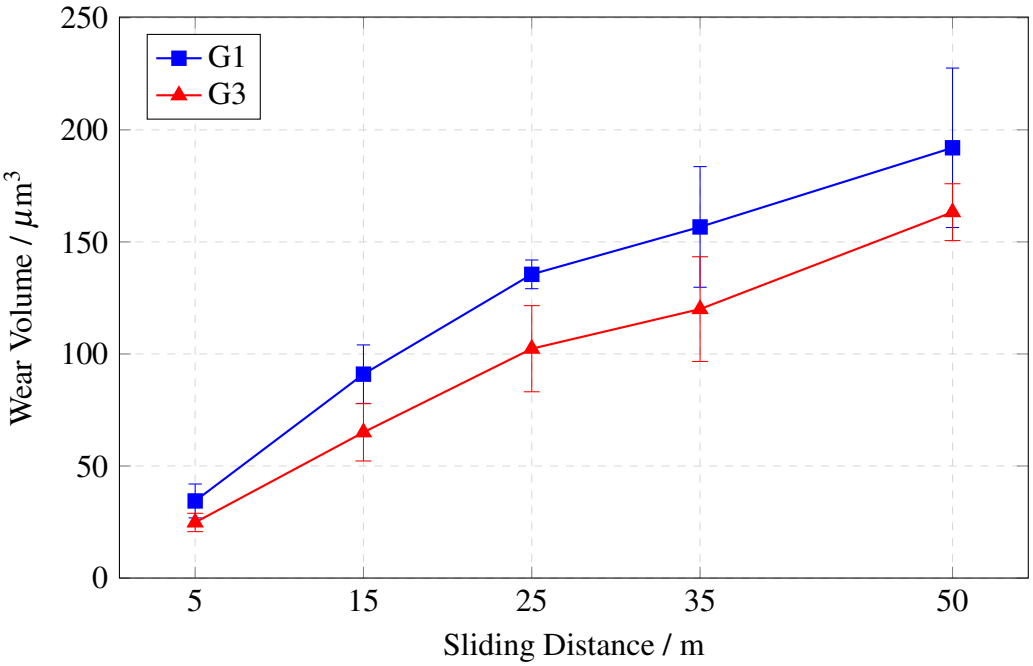


Figure 3.1. Evolution of wear volume as a function of sliding distance for materials G1 and G3. Error bars represent the expanded uncertainty (U) with a 95% confidence interval.

As illustrated in Figure 3.1, both materials exhibit a continuous, progressive increase in wear volume as the sliding distance accumulates. The evolution of wear follows a distinct biphasic behavior. A rapid initial accumulation is evident up to approximately 25 m, representing the transient *running-in* phase, which is driven by the severe shearing and progressive removal of native surface macro-asperities. Beyond the 25 m mark, the wear process does not halt; rather, the slope of both curves decreases and stabilizes. This inflection indicates that the initial roughness has been smoothed out and the tribological system has transitioned into a *stable* wear regime.

Comparing the two glass-ceramic composites, material G3 systematically demonstrates lower wear volumes than G1 across the entire experimental range, visually confirming its superior overall wear resistance. A critical observation is the near-parallel trajectory of the two curves during the stable phase. The volumetric gap (vertical distance) between G1 and G3 is established very early during the initial running-in and remains relatively constant as the test progresses, without the lines ever crossing or converging.

An analysis of the data dispersion, represented by the 95% confidence intervals (error bars), provides further insight into the damage mechanics. At short distances (e.g., 5 m), the uncertainty bands are reduced and the mean values of the two materials are relatively close, leading to a slight visual overlap. However, at greater distances (from 25 m to 50 m), a broader dispersion emerges, particularly in the G1 series, causing the error bars to elongate. This widening of the uncertainty bands is a typical tribological phenomenon attributable to the stochastic nature of brittle micro-cracking, third-body abrasion from accumulated debris, and macroscopic modifications of the contact area. Nevertheless, despite the increased variability in the later stages, the physical gap between the two trends becomes pronounced enough to maintain a clear and distinct separation between their performances.

3.2 Linear Regression

To quantify the wear kinetics of the two materials, separate linear regression analyses were performed on the running-in phase (5 m – 25 m) and the stable phase (25 m – 50 m), consistent with the piecewise-linear approximation adopted for the evolution of V_{eff} with sliding distance. For each phase, the regression provides the slope (corresponding to the local Archard wear rate), the intercept, the standard error of the regression (S), the coefficient of determination (R^2), and the associated p-value, summarised in Table 3.5. For the running-in phase, the intercept was forced to zero, consistent with the assumption of negligible wear volume at the onset of sliding.

Table 3.5. Summary of the linear regression analyses for the running-in (5 m – 25 m) and stable (25 m –50 m) wear phases.

Material	**Phase (Distance)**	**Slope** [μm^3/m]	**Intercept** [μm^3]	S	R^2 **(%)**	p**-value**
G1	Running-in (5 m – 25 m)	5.623	0*	9.58	99.12	< 0.001
	Stable (25 m – 50 m)	2.273	77.98	20.87	61.70	0.012
G3	Running-in (5 m – 25 m)	4.181	0*	10.61	98.08	< 0.001
	Stable (25 m – 50 m)	2.473	37.89	15.60	77.33	0.002

*Intercept forced to zero for the initial running-in phase.

3.2.1 Verification of Function Continuity at 25 m

In order to evaluate the continuity of the wear function at the transition point between the *running-in* and *stable* phases, the trace values were calculated for the distance $L = 25$ m using the models extracted from the linear regressions.

Table 3.6. Verification of function continuity between samples at the transition point ($L = 25$ m).

Extracted Equation	**Model Type**	**Calculation (with $L = 25$ m)**	**Trace Value at 25 m** [μm^3]
		Material G1	
trace = $5.623 \times$ distance	Without intercept	5.623×25	**140.58**
trace = $77.98 + 2.273 \times$ distance	With intercept	$77.98 + (2.273 \times 25)$	**134.81**
		Difference (Δ)*:*	5.77
		Material G3	
trace = $4.181 \times$ distance	Without intercept	4.181×25	**104.53**
trace = $37.89 + 2.473 \times$ distance	With intercept	$37.89 + (2.473 \times 25)$	**99.72**
		Difference (Δ)*:*	4.81

As can be seen from the results in Table 3.6, there is a slight deviation (5.77 μm^3 and 4.81 μm^3, respectively) between the values calculated with the no-intercept model (valid for the 5 m – 25 m interval) and those calculated with the intercept model (valid for the 25 m – 50 m interval). This difference quantifies the discontinuity of the function at the transition point between the two wear phases.

3.3 Statistical Analysis of Wear Rates: Two-Sample t-tests

To rigorously verify the presence of a transition in the wear regime at the 25 m mark, two-sample t-tests were conducted on the wear rate coefficients for both materials. The statistical analyses compared the slope of the transient *running-in* phase against the slope of the *stable* phase for series G1 and G3 independently. As summarized in Tables 3.7 and 3.8, the evaluations yield mean reductions of 3.350 $\mu m^3/m$ (with a 95% confidence interval from 2.820 to 3.880 $\mu m^3/m$) for G1 and 1.708 $\mu m^3/m$ (with a 95% confidence interval from 1.302 to 2.114 $\mu m^3/m$) for G3. Because both confidence intervals are strictly positive, exclude zero, and are corroborated by highly significant p-values of < 0.001, the null hypotheses of equal means are definitively rejected for both composites. These metrics provide robust statistical confirmation that a genuine and effective change in the wear trend occurs at the 25 m threshold across both materials. Consequently, the recorded deviations establish that the transition from a severe initial wear rate to a stabilized long-term regime is a systematic, structural characteristic of the tribological system rather than a product of random experimental fluctuations.

Table 3.7. Two-sample t-test evaluating the change in wear rate at the 25 m mark for material G1.

Statistic	**Running-in**	**Stable**
N	9	9
Mean [$\mu m^3/m$]	5.623	2.273
StDev [$\mu m^3/m$]	0.187	0.677
SE Mean [$\mu m^3/m$]	0.062	0.230
Difference ($\mu_1 - \mu_2$) [$\mu m^3/m$]	3.350	
95% CI for Difference [$\mu m^3/m$]	(2.820, 3.880)	
t-Value	14.31 (DF = 9)	
p-Value	< 0.001	

Table 3.8. Two-sample t-test evaluating the change in wear rate at the 25 m mark for material G3.

Statistic	**Running-in**	**Stable**
N	9	9
Mean [$\mu m^3/m$]	4.181	2.473
StDev [$\mu m^3/m$]	0.207	0.506
SE Mean [$\mu m^3/m$]	0.069	0.170
Difference ($\mu_1 - \mu_2$) [$\mu m^3/m$]	1.708	
95% CI for Difference [$\mu m^3/m$]	(1.302, 2.114)	
t-Value	9.37 (DF = 10)	
p-Value	< 0.001	

A direct comparison between the initial wear coefficients of G1 and G3 was subsequently performed via a two-sample t-test to evaluate whether the material type significantly influences performance during the initial *running-in* phase (0 m – 25 m). As summarized in Table 3.9, the analysis reveals a mean difference of 1.4420 $\mu m^3/m$ between the two materials, accompanied

by a 95% confidence interval spanning from 1.2438 $\mu m^3/m$ to 1.6402 $\mu m^3/m$. Since this entire range remains well above zero and the test yields a highly significant p-value of < 0.001, the null hypothesis is safely rejected. These findings provide clear statistical evidence that the chemical and microstructural differences between the composites directly impact the wear rate during the first 25 m of sliding. The observed divergence reflects a systematic variation in tribological behavior rather than experimental scatter, confirming that material G3 exhibits superior wear resistance compared to G1 throughout the transient running-in stage.

Table 3.9. Two-sample t-test evaluating the effect of the material on the wear rate during the initial running-in phase (0 m – 25 m).

Statistic	**G1**	**G3**
N	9	9
Mean [$\mu m^3/m$]	5.623	4.181
StDev [$\mu m^3/m$]	0.187	0.207
SE Mean [$\mu m^3/m$]	0.062	0.069
Difference ($\mu_1 - \mu_2$) [$\mu m^3/m$]	1.4420	
95% CI for Difference [$\mu m^3/m$]	(1.2438, 1.6402)	
t-Value	15.51 (DF = 15)	
p-Value	< 0.001	

To determine whether the material type continues to influence the wear rate during the *stable* phase (25 m – 50 m), a final two-sample t-test was conducted comparing the stabilized wear coefficients of G1 and G3. As summarized in Table 3.10, the statistical analysis indicates a minor mean difference of merely -0.200 $\mu m^3/m$ between the two samples, with a 95% confidence interval ranging from -0.804 $\mu m^3/m$ to 0.404 $\mu m^3/m$. Crucially, because this interval encompasses zero and is supported by a remarkably high p-value of 0.489, well above the conventional 0.05 threshold, the test fails to reject the null hypothesis. These findings mathematically confirm that the material type no longer has a significant effect on the wear rate once the stable regime is reached. The slight variation recorded between the two composites is insufficient to demonstrate a true mechanical difference and can be entirely attributed to normal random fluctuations inherent in the experimental process. This outcome validates the observation that, despite the pronounced differences during the initial surface conditioning, both materials ultimately settle into an equivalent, long-term wear behavior.

Table 3.10. Two-sample t-test evaluating the effect of the material on the wear rate during the stable phase (25 m – 50 m).

Statistic	**G1**	**G3**
N	9	9
Mean [$\mu m^3/m$]	2.273	2.473
StDev [$\mu m^3/m$]	0.677	0.506
SE Mean [$\mu m^3/m$]	0.230	0.170
Difference ($\mu_1 - \mu_2$) [$\mu m^3/m$]	-0.200	
95% CI for Difference [$\mu m^3/m$]	(-0.804, 0.404)	
t-Value	-0.71 (DF = 14)	
p-Value	0.489	

3.4 Friction Coefficient and Uncertainty Analysis

To complement the wear volume analysis, the coefficient of friction (μ) was examined as a function of sliding distance for both materials. For each sliding distance, the mean value of μ and its associated uncertainty were computed, following an uncertainty propagation approach analogous to the one adopted for the wear volume measurements, combining the variability observed across replicates with the instrumental measurement uncertainty. The resulting values, reported in Table 3.11 (the complete set of raw experimental data used for these calculations is available in Appendix B) and plotted with their expanded uncertainty (95% CI) in Figure 3.2, show that μ remains remarkably stable across the entire tested range (5 m – 50 m) for both materials, fluctuating within a narrow band without displaying any clear increasing or decreasing trend. This behaviour is a favourable outcome for the present study: since μ is not observed to vary systematically with sliding distance, the transition from the running-in to the stable wear regime identified in the wear volume data can be attributed to a genuine evolution of the material's structural and topographical response to sliding, rather than to a shift in the frictional loading conditions during the test. One anomalous replicate was identified for material G3 at 15 m; Figure 3.3 presents the same analysis after excluding this outlier, confirming that the apparent fluctuation was merely an artefact of this single measurement, and that the overall trend is indeed stable.

Table 3.11. Mean friction coefficient and associated measurement uncertainties for materials G1 and G3 at different sliding distances.

Material	**Distance [m]**	**Mean [-]**	u_{mes} **[-]**	U **[-]**	$U_{\%}$ **[%]**
G1	5	0.7950	0.0300	0.0638	0.08
	15	0.7170	0.0308	0.1927	0.27
	25	0.8073	0.0168	0.0249	0.03
	35	0.7835	0.0351	0.0710	0.09
	50	0.7827	0.0282	0.0382	0.05
G3	5	0.7673	0.0358	0.0613	0.08
	15	0.5220	0.0271	0.3941	0.76
	25	0.7485	0.0133	0.0660	0.09
	35	0.7295	0.0116	0.1041	0.14
	50	0.7807	0.0248	0.0400	0.05

The tabulated values are reported graphically in Figures 3.2 and 3.3 below, where the stability of μ across the tested sliding distances can be visually appreciated for both materials.

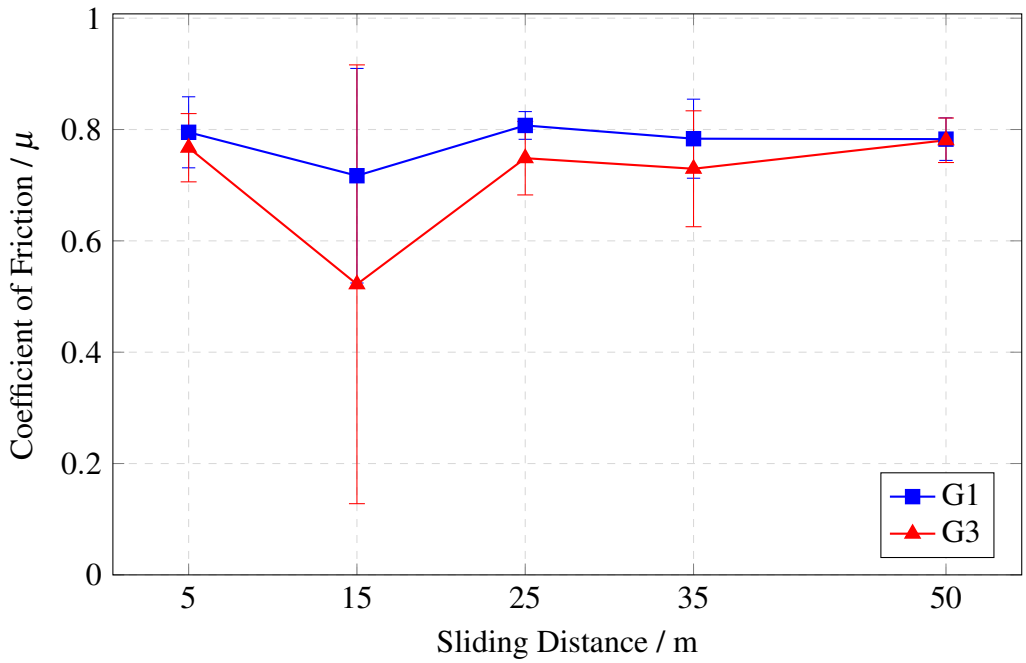


Figure 3.2. Evolution of the coefficient of friction μ as a function of sliding distance for materials G1 and G3. Error bars represent the expanded uncertainty U with a 95% confidence interval.

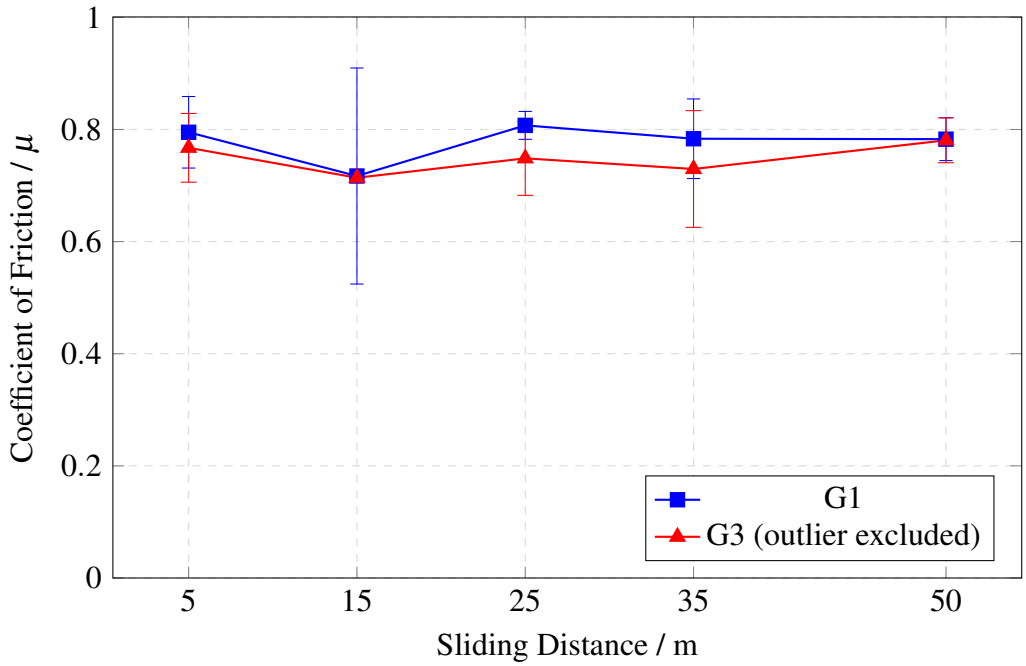


Figure 3.3. Evolution of the coefficient of friction (μ) as a function of sliding distance for materials G1 and G3, after excluding the anomalous replicate G3_3 at 15 m. Error bars represent the expanded uncertainty (U) with a 95% confidence interval; the error bar at 15 m for G3 is omitted, as the uncertainty could not be reliably estimated from the remaining two replicates.

3.5 Statistical Analysis of Friction: Two-Way ANOVA

While the volumetric wear analysis revealed significant dependencies on both sliding distance and material type, the tribological characterization of the coefficient of friction (μ) yields a distinctly different behavior. To statistically evaluate the evolution of the friction coefficient, a two-way Analysis of Variance (ANOVA) was performed, considering the sliding distance and the material type as fixed factors.

Table 3.12. Two-way ANOVA evaluating the effects of sliding distance and material type on the coefficient of friction.

Source	**DF**	**Adj SS**	**Adj MS**	**F-Value**	**p-Value**
Distance	4	0.11765	0.029413	1.98	0.129
Material	1	0.03417	0.034165	2.31	0.142
Error	24	0.35572	0.014822		
Lack-of-Fit	4	0.03359	0.008398	0.52	0.721
Pure Error	20	0.32213	0.016106		
Total	29	0.50754			

As presented in Table 3.12, the analysis reveals high p-values for both the sliding distance ($p = 0.129$) and the material type ($p = 0.142$). Since both values substantially exceed the conventional 0.05 significance level, the null hypotheses cannot be rejected. This statistically confirms that the coefficient of friction remains remarkably stable throughout the duration of the test and exhibits no significant difference between the G1 and G3 glass-ceramic composites. From a tribological perspective, this is a crucial finding. It demonstrates that the severe discrepancy in wear volumes observed during the initial *running-in* phase is not driven by differences in the macroscopic tangential friction forces, which remain statistically equivalent. Instead, the diverse wear rates must be entirely attributed to the intrinsic microstructural properties of the materials and their initial topographical features, such as the shearing of native asperities and brittle micro-cracking mechanisms.

Chapter 4

Conclusion

In conclusion, the experimental characterization of the glass-ceramic composites revealed a distinct biphasic wear behavior for both tested materials, characterized by a severe initial *running-in* phase (0 m – 25 m) followed by a stabilized *stable* regime (25 m – 50 m). Overall, material G3 demonstrated superior wear resistance, accumulating significantly less wear volume compared to G1. Statistical analysis confirmed that this performance gap is almost entirely established during the first 25 m of sliding.

This pronounced initial divergence could be primarily attributed to the differences in native surface topography. As highlighted by the preliminary roughness analysis, the distinct initial surface finishes dictate the severity of the running-in phase: the shearing, plastic deformation, and brittle fracture of the native macro-asperities may govern the rapid initial volume loss before the contact area adapts.

The statistical evaluation of the coefficient of friction demonstrated that the tangential forces remain statistically equivalent between G1 and G3 across the entire experimental range. Since the macroscopic friction does not vary between the two materials, it cannot explain why G3 wears less. Consequently, the superior durability of G3 does not appear to be driven by a lower resistance to sliding, but may instead arise from differences in the materials' intrinsic microstructural response to contact stresses and their specific initial surface conditioning, which could collectively minimize damage accumulation before the tribological system reaches equilibrium. Confirming this hypothesis, however, would require further investigation for instance through cross-sectional or fractographic analysis to directly characterize the microstructural response of each material.

Despite featuring more pronounced initial macro-asperities, material G3 effectively resists the initial contact stresses, resulting in a significantly lower rate of material removal compared to G1. Conversely, the smoother native surface of G1 does not prevent it from suffering more severe initial damage, likely due to a less resilient microstructural response to localized shear stresses. This could explains why the extent of damage in the transient *running-in* phase is so strongly material-dependent, before the inevitable mutual conditioning of the interfaces leads the system to settle into a *stable* wear regime governed by equivalent mechanisms.

Bibliography

[1] Maha Fouad1 and Eman Allam. Failures in fixed dental prostheses: A clinical survey on causes and longevity. *Journal of Dental Science Research*, 2024.

[2] Pajares A. Constantino P. Lawn B.R. Borrero-Lopez, O. A model for predicting wear rates in tooth enamel. *Journal of the Mechanical Behavior of Biomedical Materials*, 2014.

[3] Yu Zhangb Brian R. Lawn Oscar Borrero-Lopez, Fernando Guiberteau. Wear of ceramic-based dental materials. *Journal of the Mechanical Behavior of Biomedical Materials*, 2019.

[4] Giacomo Maculotti, Edoardo Goti, Gianfranco Genta, Luigi Mazza, and Maurizio Galetto. Uncertainty-based comparison of conventional and surface topography-based methods for wear volume evaluation in pin-on-disc tribological test. *Tribology International*, 2022.

[5] Braem M. Vuylsteke-Wauters M. Vanherle G. Lambrechts, P. Quantitative in vivo wear of human enamel. *Journal of Dental Research*, 1989.

[6] Bush M.B. Ford-C. Lee J.J.-W. Constantino P.J. Lawn B.R. Keown, A. Fracture susceptibility of worn teeth. *Journal of the Mechanical Behavior of Biomedical Materials*, 2012.

[7] M.J.MORA* C.CADARSO-SUAREZ U.SANTANA B.RILO, N.FERNANDEZ-FORMOSO. Distance of the contact glide in the closing masticatory stroke during mastication of three types of food. *Journal of Oral Rehabilitation*, 2009.

[8] Célio Gabriel Figueiredo-Pina, Ana Catarina Branco, Rogério Colaço, and Ana Paula Serro. A state-of-the-art review on the wear of the surfaces of natural teeth and prosthetic crowns. *MDPI Journal*, 2020.

[9] Jamie J. Kruzic, Mark Hoffman, and Joseph A. Arsecularatne. Fatigue and wear of human tooth enamel: A review. *Journal of the Mechanical Behavior of Biomedical Materials*, 2023.

[10] Giovanni Strafellini. *Friction and Wear*. Springer, 2015.

[11] Giacomo Maculotti. Title of the course or specific lecture topic. Lecture notes, Politecnico di Torino. Unpublished material, 2026.

[12] Z R Zhou Oscar Borrero-Lopez, Fernando Guiberteau and J Zheng. Tribology of dental materials: a review. *Journal of Physics D: Applied Physics*, 2008.

[13] Franz-Xaver REICHL Siegward D. HEINTZE and Reinhard HICKEL. Wear of dental materials: Clinical significance and laboratory wear simulation methods —a review. *Dental Materials Journal*, 2019.

[14] Julie A. Holloway Kuljirarnat Jitwirachot, Pimduen Rungsiyakull and Wissanee Jiamahasap. Wear behavior of different generations of zirconia:present literature. *International Journal of Dentistry*, 2022.

[15] Hugo R. Fernandes, Dilshat U. Tulyaganov, Ashutosh Goel, Manuel J. Ribeiro, Maria J. Pascual, and José M.F. Ferreira. Effect of al2o3 and k2o content on structure, properties and devitrification of glasses in the li2o–sio2 system. *Journal of the European Ceramic Society*, 2010.

[16] Konstantinos Dimitriadis c Saidazim Murtazaev d Simeon Agathopoulos e Hugo R. Fernandes b Dilshat U. Tulyaganov a, Manuel F.R.P. Alves b. Fundamentals and advances in production and application of non-stoichiometric lithium disilicate glass-ceramics: A brief review. *Ceramics International*.

[17] Giacomo Maculotti, Edoardo Goti, Gianfranco Genta, Luigi Mazza, and Maurizio Galetto. Comprehensive mechanical and tribological characterization of metal-polymer ptfe+pb/bronze coating by in-situ electrical contact resistance measurement augmented tribo-mechanical tests. *Tribology International*, 2024.

[18] International Organization for Standardization. Geometrical product specifications (gps) — surface texture: Areal part 700: Calibration, adjustment and verification of areal topography measuring instruments. 2022.

Appendix A

Experimental Wear Data Tables

This appendix contains the detailed experimental data regarding the calculated displaced volumes (V_p) and removed wear volumes (V_r) for all the sample series tested under linear sliding motion with the relative measurement uncertainty. The values were obtained through the subtraction of pre-test and post-test 3D surface topographies.

A.1 Sample Series G1

Table A.1. Experimental displaced volumes (V_p) and removed wear volumes (V_r) evaluated at different sliding distances under a 10 N normal load.

*G*1_2 **Sample Series**				
Sliding Distance	**Displaced Volume**		**Removed Volume**	
[m]	**Value [μm^3]**	**Uncert. [μm^3]**	**Value [μm^3]**	**Uncert. [μm^3]**
5	0.2775	0.0002	41.5839	0.0313
15	1.1002	0.0008	102.7022	0.0704
25	3.8381	0.0029	125.3432	0.0934
35	13.3077	0.0091	149.0163	0.1022
50	8.1264	0.0056	205.5187	0.1409

Table A.2. Experimental displaced volumes (V_p) and removed wear volumes (V_r) evaluated at different sliding distances under a 10 N normal load.

*G*1_3 **Sample Series**				
Sliding Distance	**Displaced Volume**		**Removed Volume**	
[m]	**Value [μm^3]**	**Uncert. [μm^3]**	**Value [μm^3]**	**Uncert. [μm^3]**
5	0.9204	0.0006	28.6781	0.0187
15	0.4746	0.0003	81.953	0.0533
25	0.237	0.0001	137.7601	0.0853
35	0.3898	0.0002	176.2724	0.1092
50	0.4463	0.0003	156.2838	0.0968

Table A.3. Experimental displaced volumes (V_p) and removed wear volumes (V_r) evaluated at different sliding distances under a 10 N normal load.

*G*1_4 **Sample Series**				
Sliding Distance	**Displaced Volume**		**Removed Volume**	
[m]	**Value [μm^3]**	**Uncert. [μm^3]**	**Value [μm^3]**	**Uncert. [μm^3]**
5	5.3231	0.0034	26.4497	0.0169
15	4.07	0.0034	82.6472	0.0527
25	0.0726	0	139.348	0.0889
35	3.913	0.0025	127.1551	0.0811
50	2.9779	0.0019	202.6623	0.1292

A.2 Sample Series G3

Table A.4. Experimental displaced volumes (V_p) and removed wear volumes (V_r) evaluated at different sliding distances under a 10 N normal load.

*G*3_1 **Sample Series**				
Sliding Distance	**Displaced Volume**		**Removed Volume**	
[m]	**Value [μm^3]**	**Uncert. [μm^3]**	**Value [μm^3]**	**Uncert. [μm^3]**
5	1.6212	0.0011	24.5008	0.0159
15	0.6155	0.0004	73.821	0.0479
25	3.2184	0.0021	116.1227	0.0753
35	0.941	0.0006	128.9004	0.0836
50	0.5441	0.0004	154.9069	0.1005

Table A.5. Experimental displaced volumes (V_p) and removed wear volumes (V_r) evaluated at different sliding distances under a 10 N normal load.

*G*3_2 **Sample Series**				
Sliding Distance	**Displaced Volume**		**Removed Volume**	
[m]	**Value [μm^3]**	**Uncert. [μm^3]**	**Value [μm^3]**	**Uncert. [μm^3]**
5	1.6479	0.001	25.8613	0.0159
15	0.3086	0.0002	52.5246	0.0324
25	1.1787	0.0007	100.4289	0.0619
35	0.3511	0.0002	96.3933	0.0594
50	5.2156	0.0032	153.3324	0.0946

Table A.6. Experimental displaced volumes (V_p) and removed wear volumes (V_r) evaluated at different sliding distances under a 10 N normal load.

*G*3_3 **Sample Series**				
Sliding Distance	**Displaced Volume**		**Removed Volume**	
[m]	**Value [μm^3]**	**Uncert. [μm^3]**	**Value [μm^3]**	**Uncert. [μm^3]**
5	14.9358	0.0099	5.8497	0.0039
15	1.5263	0.001	66.296	0.0438
25	1.7998	0.0012	84.28089	0.0556
35	3.4404	0.0023	130.0414	0.0858
50	1.2198	0.0008	174.6142	0.1087

Appendix B

Experimental Friction Data Tables

This appendix contains the detailed experimental data regarding the mean coefficient of friction (μ) and its standard deviation evaluated at different sliding distances for all the sample series.

B.1 Sample Series G1

Table B.1. Mean coefficient of friction (μ) and standard deviation evaluated at different sliding distances.

*G*1_2 **Sample Series**					
μ	**5 m**	**15 m**	**25 m**	**35 m**	**50 m**
Mean	0.8454	0.8278	0.7962	0.8017	0.8001
St. Dev.	0.0097	0.0101	0.0195	0.013	0.0155

Table B.2. Mean coefficient of friction (μ) and standard deviation evaluated at different sliding distances.

*G*1_3 **Sample Series**					
μ	**5 m**	**15 m**	**25 m**	**35 m**	**50 m**
Mean	0.7854	0.7946	0.8223	0.8224	0.7653
St. Dev.	0.0405	0.0229	0.0076	0.0077	0.0288

Table B.3. Mean coefficient of friction (μ) and standard deviation evaluated at different sliding distances.

*G*1_4 **Sample Series**					
μ	**5 m**	**15 m**	**25 m**	**35 m**	**50 m**
Mean	0.7542	0.5286	0.8035	0.7264	0.7827
St. Dev.	0.0311	0.0471	0.0203	0.0589	0.0362

B.2 Sample Series G3

Table B.4. Mean coefficient of friction (μ) and standard deviation evaluated at different sliding distances.

*G*3_1 **Sample Series**					
μ	**5 m**	**15 m**	**25 m**	**35 m**	**50 m**
Mean	0.7747	0.7863	0.7964	0.7892	0.7536
St. Dev.	0.0178	0.0108	0.0072	0.0049	0.0408

Table B.5. Mean coefficient of friction (μ) and standard deviation evaluated at different sliding distances.

*G*3_2 **Sample Series**					
μ	**5 m**	**15 m**	**25 m**	**35 m**	**50 m**
Mean	0.8024	0.6416	0.7616	0.6267	0.7998
St. Dev.	0.0138	0.0233	0.0112	0.0162	0.0067

Table B.6. Mean coefficient of friction (μ) and standard deviation evaluated at different sliding distances.

*G*3_3 **Sample Series**					
μ	**5 m**	**15 m**	**25 m**	**35 m**	**50 m**
Mean	0.7249	0.1381	0.6875	0.7726	0.7888
St. Dev.	0.0577	0.0392	0.0187	0.0107	0.0118

Appendix C

Experimental Roughness Data Tables

Table C.1. Surface roughness parameters (S_q and S_a) evaluated for the two sample series.

G1			G3		
Sample	S_q **[μm]**	S_a **[μm]**	**Sample**	S_q **[μm]**	S_a **[μm]**
1	0.09184	0.069820	1	0.83598	0.629470
2	0.14313	0.109424	2	0.91782	0.671463
3	0.11571	0.081070	3	1.26052	0.740089
4	0.12351	0.064989	4	2.12255	0.920534
5	0.11000	0.070836	5	1.37479	0.820262
6	0.13030	0.085591	6	0.80060	0.571251
7	0.13953	0.089068	7	1.52776	0.592546
8	0.17436	0.114560	8	0.89603	0.615275
9	0.10734	0.069553	9	0.82662	0.551733
10	0.10040	0.072798	10	1.48379	0.586426
11	0.13781	0.092336	11	0.99352	0.621019
12	0.18248	0.125996	12	0.75865	0.549561
13	0.16188	0.110870	13	1.33932	0.834471
14	0.14956	0.111668	14	1.23738	0.928229
15	0.18555	0.122180	15	1.14059	0.813300

Note: Roughness data were acquired using a [inserisci marca] [inserisci modello] profilometer.

Appendix D

Test Setup Procedure

Prior to each wear test, the tribometer was set up according to the following procedure:

1. **Initial mounting**: the pin holder is mounted and the sample is fixed in place, ensuring it is properly clamped.
2. **Pin positioning**: for the first test on a given specimen, the pin is positioned exactly at the centre of the sample. For subsequent tests, the specimen is marked with a coloured marker beforehand, and it is verified that the pin does not rest on a pre-existing wear track. In practice, this is checked by lightly colouring the tip of the pin and briefly lowering it into contact with the specimen: viewing the sample surface at eye level with the reference plane makes it possible to clearly identify whether the pin is positioned over a previous track.
3. **Contact with the sample**: with no weights loaded, the arm is set to the middle position; the screw securing the pin is then loosened, and the pin is gently lowered until it makes contact with the specimen surface.
4. **Weight application**: the arm is raised to the up position and, while held in this position, the test weights are applied.
5. **Software preparation**: the test procedure is initiated on the control PC and advanced up to the step immediately following the homing routine.
6. **Initial liquid application**: with the arm still in the up position, a few drops of the test liquid are applied, forming a small droplet on the contact area.
7. **Lowering the arm**: the arm is then lowered to the down position, in preparation for the start of the test.
8. **Meniscus formation**: additional drops of solution are added until a stable liquid meniscus forms between the specimen and the pin-holder insert.
9. **Test start**: the test is finally started from the control software.